HIPPOCAMPUS 22:1733–1749 (2012)

Voltage Dependence of Subthreshold Resonance Frequency in Layer II of Medial Entorhinal Cortex

Christopher F. Shay,* Ian S. Boardman, Nicholas M. James, and Michael E. Hasselmo

ABSTRACT: The resonance properties of individual neurons in entorhinal cortex (EC) may contribute to their functional properties in awake, behaving rats. Models propose that entorhinal grid cells could arise from shifts in the intrinsic frequency of neurons caused by changes in membrane potential owing to depolarizing input from neurons coding velocity. To test for potential changes in intrinsic frequency, we measured the resonance properties of neurons at different membrane potentials in neurons in medial and lateral EC. In medial entorhinal neurons, the resonant frequency of individual neurons decreased in a linear manner as the membrane potential was depolarized between −70 and −55 mV. At more hyperpolarized membrane potentials, cells asymptotically approached a maximum resonance frequency. Consistent with the previous studies, near resting potential, the cells of the medial EC possessed a decreasing gradient of resonance frequency along the dorsal to ventral axis, and cells of the lateral EC lacked resonant properties, regardless of membrane potential or position along the medial to lateral axis within lateral EC. Application of 10 μM ZD7288, the H-channel blocker, abolished all resonant properties in MEC cells, and resulted in physiological properties very similar to lateral EC cells. These results on resonant properties show a clear change in frequency response with depolarization that could contribute to the generation of grid cell firing properties in the medial EC. © **2012 Wiley Periodicals, Inc.**

KEY WORDS: grid cells; stellate cells; lateral entorhinal cortex; spatial navigation; oscillatory interference

INTRODUCTION

The entorhinal cortex (EC) plays an important role in spatial memory function, as shown by impairments of spatial memory with lesions of this structure (Steffanach et al., 2005; Moser and Moser, 2008). Spatial coding by medial EC has been shown in unit recordings of layer II medial EC "grid cells," which fire when a rat is in a repeating array of spatial locations falling on a hexagonal grid (Fyhn et al., 2004; Hafting et al., 2005; Moser and Moser, 2008). Computational models of the mechanism of the generation of entorhinal grid cells (Burgess et al., 2007) have proposed a role for intrinsic properties of entorhinal neurons that were initially discovered in slice preparations. Layer II of medial EC contains stellate cells that display subthreshold membrane potential oscillations (MPO) (Alonso and Llinas, 1989; Klink and Alonso, 1993) and membrane potential resonance (Haas and White, 2002; Erchova et al., 2004; Giocomo et al., 2007). Differences in the resonance properties of individual entorhinal neurons may underlie differences in the spacing and size of grid cell firing fields that have been found to increase along the dorsal to ventral (*D*/*V*) axis of the medial EC (Hafting et al., 2005; Sargolini et al., 2006). In vitro slice studies (Giocomo et al., 2007; Giocomo and Hasselmo, 2008a,b; Boehlen et al., 2010; Dodson et al., 2011) have found similar gradients in MPO frequencies and resonant frequencies along the *D*/*V* axis of the medial EC.

An initial model of grid cells developed by Burgess et al. used oscillatory interference between oscillations with differences in frequency (Burgess et al., 2005; Blair et al., 2007; Burgess et al., 2007; Hasselmo et al., 2007; Blair et al., 2008; Burgess, 2008). In some versions of these models, the changes in frequency were proposed to arise from changes in membrane potential driven by cells responding to head direction and running speed (Burgess et al., 2007; Hasselmo et al., 2007), suggesting an important role of changes in intrinsic frequency with membrane potential. A number of subsequent studies have argued against an interaction of MPOs within single cells based on the variance of MPOs (Welinder et al., 2008; Giocomo and Hasselmo, 2008a; Zilli et al., 2009), the synchronization properties of MPOs (Remme et al., 2009), and the lack of linear changes in MPO frequency with membrane potential (Yoshida et al., 2011). However, models have not yet demonstrated the reason why the intrinsic resonance of neurons appears to correlate with the spacing and size of grid cell firing fields.

As an alternative to MPOs, differences in resonance frequency at different membrane potentials may contribute to the generation of grid cells. The membrane potential dependence of resonance in EC is unclear. An initial study did not find resonance to depend on membrane potential (Erchova et al., 2004), but subsequent studies have shown membrane potential dependence (Nolan et al., 2007; Boehlen et al., 2010; Heys et al., 2010). These studies plotted only three different membrane potentials, leaving the shape of the change in resonance frequency with membrane potential unspecified. In particular, it is not clear if the change in resonance frequency with membrane potential is linear.

Center for Memory and Brain, Department of Psychology, Graduate Program for Neuroscience, Boston University, Boston, Massachusetts
Grant sponsor: National Institute of Mental Health; Grant number: R01 MH61492; Grant sponsor: The Office of Naval Research, MURI award
*Correspondence to: Christopher F. Shay, Center for Memory and Brain, Department of Psychology, Graduate Program for Neuroscience, Boston University, 2 Cummington St, Room 109, Boston, MA 02215, USA. E-mail: cshay@bu.edu
Accepted for publication 4 January 2012
DOI 10.1002/hipo.22008
Published online 27 February 2012 in Wiley Online Library (wileyonlinelibrary.com).

Oscillatory interference models require that the difference in frequency between pairs of oscillators must vary linearly with velocity. This requirement of the model could be satisfied by a linear change in resonant frequency with membrane potential.

In contrast to medial EC, grid cells have not been shown in lateral EC and recordings of spiking activity in cells of lateral EC show significantly less spatial selectivity than in medial EC (Hargreaves et al., 2005; Yoganarasimha et al., 2011). Interestingly, this difference in the presence of grid cells appears consistent with the fact that the previous studies showed that cells of the lateral EC lack subthreshold MPOs (Tahvildari and Alonso, 2005). However, a systematic approach to measuring the resonance properties of neurons to different input frequencies in lateral EC has not been published previously.

To address these issues, we measured the membrane potential dependence of the resonant frequency in layer II of medial EC and lateral EC. We found that the resonant frequency of individual cells in layer II of the medial EC showed a linear decrease in frequency as the membrane potential was depolarized. These results are important for the hypothesis that the regulation of resonant frequency by synaptic inputs influencing membrane potential could contribute to the generation of grid cells. Furthermore, they support the role of the *H*-current in resonant properties that could underlie the processing of spatial information in the medial EC. These results were presented previously as an abstract (Shay et al., 2010).

MATERIALS AND METHODS

Slice Preparation

We measured the effect of membrane potential on the resonant frequency of neurons at different positions along the *D*/*V* axis of layer II in the medial EC and the medial to lateral (*M*/*L*) axis of lateral EC. All experimental protocols were approved by the Institutional Animal Care and Use Committee at Boston University. Long–Evans rats (postnatal days 17–21, Charles River, Wilmington, MA) were deeply anesthetized with isoflurane (Abbot Laboratories). After the absence of both pedal and tail pinch reflexes, brains were rapidly removed and placed in ice-cold artificial cerebrospinal fluid (aCSF) containing (in mM) 125 NaCl, 2.0 CaCl, 2.5 KCl, 1.25 NaH_2PO_4, 25 $NaHCO_3$, 25 d-glucose, and 1.0 $MgCl_2$ (pH adjusted to 7.4 with 95% O_2–5% CO_2). Horizontal (medial and lateral EC recordings) or coronal (lateral EC recordings) brain slices, 400-μm thick, were made using a vibroslicer (Leica VT 1000). Immediately after slicing, slices were transferred to a holding chamber filled with aCSF and incubated for 30 min at 33°C. Following this incubation, slices were left at room temperature for another 30 min before recordings began.

Electrophysiological Recordings

Slices were placed in a recording chamber superfused with aCSF containing 2-mM kynurenic acid and 100 μM of picrotoxin to block glutamatergic and GABAergic synaptic transmission, respectively. The temperature was maintained between 34 and 36°C. Whole-cell pipettes were fabricated from borosilicate glass capillaries by means of a P-87 horizontal puller (Sutter Instruments). Pipettes were filled with internal solution containing (in mM) 120 K-gluconate, 10 HEPES, 0.2 EGTA, 20 KCl, 2.0 $MgCl_2$, 4.0 Na_2ATP, 0.3 Na_3GTP, and 7 phosphocreatine-diTris (pH adjusted to 7.3 with KOH). An aliquot of 0.1% biocytin was included in the internal solution for the purpose of labeling. When filled with internal solution, pipettes had resistances from 3 to 5 MΩ. Cells were visualized under an upright microscope (Zeiss Axioskop 2 or Olympus BX51I) equipped with a 40× immersion lens and a near infrared charge-coupled device camera (JAI CV-M50IR). Tight seals (>1 GΩ) were obtained and whole-cell access was gained by brief negative pressure. Current-clamp recordings were made with the Multi Clamp 700B amplifier (Axon Instruments) using the built-in capacitance compensation and bridge balance circuit. Signals were sampled at either 10 or 20 kHz using Clampex 9.0 (Axon Instruments).

After obtaining whole-cell configuration, cells were left to stabilize for 2–5 min before recordings began. Only cells with resting membrane potentials below −55 mV were used for this study. Additionally, all cells displayed overshooting action potentials for the entire recording session. We aimed to use only stellate cells in layer II medial EC. Therefore, we did not include cells displaying fast spiking, which is often indicative of interneurons. We also excluded pyramidal cells by measuring the sag potential in each cell. Stellate cells displayed a strong sag potential, whereas pyramidal cells did not. The sag potential was measured by delivering nine successive 0.5 s, 50 pA hyperpolarizing current steps with cells held at −65 mV. All cells of lateral EC, recorded from both horizontal and coronal sections, lacked a strong sag potential, making it more difficult to distinguish between cell types. The physiology of layer II lateral EC cells was similar (especially in coronal sections), but the morphology of every cell is not known. Therefore, it is possible that all morphological cell types are included in the lateral EC data set. However, the fills that we did obtain showed that cells in lateral EC were fan cells according to Tahvildari and Alonso, 2005.

To assess the resonant properties of medial and lateral EC cells, the chirp function in Matlab® (Natick, MA Version 7.9, 2009) was used to create an impedance amplitude profile (ZAP) stimulus (Erchova et al., 2004). The ZAP consisted of a 20-s sinusoid with linearly increasing frequency (0–20 Hz). The peak-to-peak amplitude of the ZAP stimulus ranged from 40 to 120 pA and was adjusted so as to maintain subthreshold membrane potential dynamics across the range of membrane potentials (−55 to −70 mV: medial EC, $n = 65$ and lateral EC horizontal, $n = 21$; −55 to −80 mV: medial EC, $n = 17$; and −60 to −90 mV: medial EC, $n = 7$ and lateral EC coronal, $n = 43$) where resonant frequencies were measured. Therefore, the smaller 40 pA ZAP stimulus was used at depolarized values (−55 to −60 mV), whereas the larger amplitude stimuli were used at more hyperpolarized potentials. This pro-

cedure accomplished two things. First, it ensured that spiking was not elicited and second, it allowed for sufficiently large voltage responses to clearly measure the resonant frequency at all membrane potentials. Additional experiments showed that there were no significant differences in resonant frequency measured with a full range of different ZAP amplitudes.

Cell Anatomical Locations

The relative anatomical (*D*/*V* or rostral to caudal, *R*/*C*) location of each cell was determined by keeping track of the depth of each slice. Brains were sliced from either the dorsal or the ventral surface (horizontal slices) or from the caudal surface (coronal slices). At the start of slicing, an initial slice with the vibratome was made that was between 2 and 3 mm from the surface of the brain. The relative distance of each slice was then calculated by keeping track of the number of slices taken (400 μm each) and adding that to the depth of the initial cut. Each slice was placed in a labeled holding chamber, designed to keep slices separate from one another. In horizontal sections, medial EC recordings were made between 2.8 and 7.8 mm from the dorsal surface, whereas recordings in lateral EC were taken between 4.5 and 7.8 mm. In coronal sections, recordings were made in lateral EC between 2.2 and 4.6 mm from the caudal surface of the brain. To measure the distance from each cell and either the caudomedial tip (horizontal sections) or the rhinal sulcus (coronal sections), we used the coordinates of the micromanipulator of both locations. All distances reported were calculated by finding the length of the hypotenuse between the cell and the appropriate anatomical landmark. In horizontal slices, we recorded from cells ranging from 0.5 to 2.6 mm from the most caudomedial aspect of the slice. We tended to stay closer to the caudomedial tip of the slice in ventral slices as a substantial portion of lateral EC is included at these depths. In more dorsal slices (between 2.5 to 5.8 mm from the dorsal surface), we recorded from cells up to 2.5 mm because lateral EC is limited at these *D*/*V* locations. In coronal slices, all cells were located ventral to the rhinal sulcus and ranged from 0.386 to 1.925 mm from the center of the rhinal sulcus. Initially, biocytin staining was performed to ensure cell type and anatomical location within the slice. This staining method has been described previously (Giocomo and Hasselmo, 2009). About 16% of all cells (11/65 medial EC, 4/21 LEC-horizontal, and 10/43 LEC-coronal) were processed for biocytin fills.

We also mapped recording sites along the *D*/*V* axis of medial EC and the *M*/*L* axis of lateral EC. To do this, brains were sliced at 200 μm, fixed in 4% formaldehyde for 2 h, washed in 0.1 M PBS, and Nissl stained. Using the above measurements, we measured the hypotenuse length of right triangles from appropriate landmarks of representative horizontal and coronal slices along the *D*/*V* and *R*/*C* axis, respectively. Measuring the *R*/*C* position of a slice as well as the *D*/*V* (i.e. the distance from the center of the rhinal sulcus) position of a cell within a slice provides an accurate measure of a cell's position along the *M*/*L* axis of lateral EC. Therefore, throughout this article, the use of *D*/*V* in reference to lateral EC is meant as a measurement within a single slice representing the distance of a cell from the center of the rhinal sulcus.

Data Analysis

The sag potential amplitude was calculated using Matlab® by subtracting the steady-state potential from the most negative voltage of the sag amplitude. This was performed with a 95% confidence interval for all hyperpolarizing current steps in medial and lateral EC cells.

Resonant frequencies were calculated following the techniques from Erchova (Erchova et al., 2004) using a RLC model and Matlab® curve fitting routines. A characteristic resonant response of the cell to the ZAP input waveform was observed as a peak in the excursions of the membrane potential waveform (maximum range of the envelope), which occurs at the time in the data when the instantaneous frequency of the ZAP signal was near the cell's resonant frequency. Taking the impedance [$Z(f)$] of the cell as the ratio of the magnitude of the Fourier transform of the output (membrane potential) to the magnitude of the Fourier transform of the input (ZAP plus dc injection), there was usually a peak in the impedance curve somewhere in the ZAP frequency range (0–20 Hz) at different levels of mean membrane potential.

The impedance response can be accurately modeled with a passive circuit model (RLC) as described by Erchova et al. (2004). Applying their model in the Matlab® lsqcurvefit routine, we obtained the resonance frequency (F_r) as that frequency in the range of 0.5–16 Hz that gives an RLC model fit that is maximal. The quality ratio (Q) is taken as the ratio of the corresponding maximum impedance to the RLC model value at zero frequency.

Biophysical Simulation Methods

We tested whether the relationship of resonance frequency to mean membrane potential observed in the in vitro data from medial EC stellate cells could be derived from the voltage dependence of the kinetics of the ion channels theorized to support the resonance. We performed biophysical simulations in Matlab® (version 7.9, 2009) to analyze channel behavior under the stimulus protocol and to analyze how biophysical properties affect the dependence of resonance frequency on membrane potential. A single compartmental model of a stellate cell was constructed. Similar to the previous models (Fransén et al., 2004; Heys et al., 2010), the system contains currents previously proposed to underlie subthreshold MPOs (SMPO), these being the hyperpolarization-activated cation current, $\mathbf{I_h}$, and persistent sodium current, $\mathbf{I_{NaP}}$. These mechanisms have also been analyzed in other models (White et al., 1995; Dickson et al., 2000). For fast spiking simulations, we included Hodgkin–Huxley currents $\mathbf{I_{Na}}$ (fast sodium channel) and $\mathbf{I_K}$ (delayed rectifier) with parameters from a model of a CA3 pyramidal neuron (Traub et al., 1991). All currents were modeled using the Hodgkin–Huxley formalism in an equivalent circuit representation of membrane potential dynamics as follows:

$$C_{\mathrm{m}}\frac{dV_{\mathrm{m}}}{dt}=\sum_i g_i(V_{\mathrm{m}})(V_{\mathrm{m}}-E_i)+I_{\mathrm{noise}}+I_{\mathrm{app}}+I_L$$

In this first-order dynamical system, V_{m} is the membrane potential variable and C_{m} is the membrane capacitance constant (1 mF/cm^2). The term in the right-hand side summation includes the currents listed above, each with reversal potentials E_i and with voltage-dependent conductance gating variables g_i incorporating the corresponding channel kinetics. Also, included in the summation is leakage current $\mathbf{I_L}$ which has constant conductance. Noise current $\mathbf{I_{noise}}$ is introduced using a voltage-independent, normally distributed, conductance noise. The remaining term $\mathbf{I_{app}}$ represents the injected current for testing resonance at different membrane potentials. In our simulations, the injected current is the sum of the ZAP described above for testing the resonance peak and a baseline direct current level, which has a negative sign to hyperpolarize and a positive sign to depolarize the cell for testing the resonance at different mean membrane potentials.

In general, the voltage-dependent gating variables g_i are proportional to the product of the corresponding channel activation and inactivation probabilities,

$$g_i(V)=G_i m_i(V)h_i(V)$$

where G_i is the maximum conductance density for the channel; and, m_i and h_i are the probability of channel activation or inactivation, respectively, each following (by integration) a variable long-term value at a variable rate,

$$\frac{dp}{dt}=\tau_p^{-1}(p_\infty-p)$$

where p_∞ is the voltage-dependent long-term (steady state) value of activation or inactivation, and τ_p is the corresponding, voltage-dependent, integration time constant. In our system, only fast sodium current I_{Na} was modeled with continuous functions for both activation and inactivation probabilities. In addition, the fast sodium activation probability was moderated in its contribution to I_{Na} by squaring (Traub et al., 1991).

The kinetics of the persistent sodium current were modeled according to Fransén et al., (2004) for activation, and according to Magistretti and Alonso, (1999) for inactivation. The fast time scale of activation permitted simplification by setting the activation directly to its steady-state value for the current membrane potential at each time step. The *H*-current is modeled with fast and slow activation time constants (Fransén et al., 2004). The Matlab® curve fitting tool was used to fit the time constant and the steady-state activation functions to experimental voltage clamp data for both dorsal and ventral stellate cells (Giocomo and Hasselmo, 2008a).

The differential equations in the above system were integrated using a Matlab® ODE solver (*ode15s* was selected for beneficial speed/accuracy trade-off compared with *ode45* or the Crank–Nicolson method). The time step used for the analysis of the solutions was 0.1 ms. For all simulations, the results presented were preceded by a 3-s equilibration interval following which, given continued fixed current input, the mean membrane potential would change $< \sim$5% per second.

Conductance Gating Models

The voltage dependence of the gating parameters for each active conductance was modeled as listed in Table 1. Voltages are in millivolts, time in milliseconds, and constant values were calculated at 37°C. The maximum conductance values G_i (mS/cm^2) for different currents had the following values: fast *H*-current, 0.13; slow *H*-current, 0.079; NaP, 0.065; leakage current, 0.07; and fast spiking: Na: 3.8, K: 10.7. The reversal potentials E_i (mV) for different currents had the following values: hyperpolarization activated nonspecific cation channel (I_{h}): −20; persistent sodium and fast sodium channels (I_{NaP}, I_{Na}): 87; delayed rectifier channel (I_{K}): −83; leakage channel (I_{L}): −90, V_{m} at rest = −60 mV. These values were chosen to give physiologically relevant membrane resistance, sag response, resonance frequency, resonance strength, SMPO frequency, and SMPO amplitude.

Resonance Characterization of the Model

A characteristic resonant response of the model to the ZAP input waveform was observed as a peak in the excursions of the simulated membrane potential waveform (maximum range of the envelope), which occurs at the time in the simulation when the instantaneous frequency of the ZAP signal was near the model's resonance frequency. The resonant frequency was calculated in the model using the same techniques used for calculating resonant frequency in the experimental data, as described in the Data Analysis section. To show the relationship of the resonant frequency to biophysical parameters of the model, the magnitude and inverse time constant of the *H*-current were also plotted for different membrane potentials.

RESULTS

Our focus in this study was to analyze the effect of differences in mean membrane potential on the resonant frequency of neurons in EC. The effect of membrane potential on resonant frequency was measured from neurons at different positions along the *D*/*V* and *M*/*L* axes in layer II of medial and lateral EC, respectively.

Figure 1 shows photographs of horizontal (Figs. 1A–D) and coronal (Figs. 1E–H) sections along the *D*/*V* and *M*/*L* axes of medial and lateral EC, respectively. Two magnifications are shown to show cell location within layer II of the slice as well as morphological detail. Cells of medial EC had radiating dendrites in all directions, resembling the morphology of stellate cells (Alonso and Klink, 1993), whereas cells of lateral EC had dendrites extending horizontally across layer II and vertically

TABLE 1.

Model Parameters

Parameters	References
I_h Fast activation	
Dorsal	
$\tau_m = 29.5/(\exp[(V_m + 99)/(-15.4)] + \exp[(V_m + 25.1)/9.64])$	Fransén et al., (2004); Giocomo and Hasselmo, (2008a)
$m_\infty = 1/(1 + \exp[(V_m + 68.1)/7.14])$	Giocomo and Hasselmo, (2008a)
Ventral	
$\tau_m = 327/(\exp[(V_m + 40.1)/(13.6)] + \exp[(V_m + 70.2)/(-23.8)])$	Fransén et al., 2004; Giocomo and Hasselmo, (2008a)
$m_\infty = 1/(1 + \exp[(V_m + 68.1)/5.46])$	Giocomo and Hasselmo, (2008a)
I_h Slow activation	
Dorsal	
$\tau_m = 357/(\exp[(V_m + 30.6)/6] + \exp[(Vm + 116)/(-41)])$	Fransén et al., (2004); Giocomo and Hasselmo, (2008a)
$m_\infty = 1/(1 + \exp[(V_m + 68.1)/7.14])$	Giocomo and Hasselmo, (2008a)
Ventral	
$\tau_m = 459/(\exp[(V_m + 39.5)/6.1] + \exp[(V_m + 90.6)/(-13.8)])$	Fransén et al., (2004); Giocomo and Hasselmo, (2008a)
$m_\infty = 1/(1 + \exp[(V_m + 66.1)/5.46])$	Giocomo and Hasselmo, (2008a)
I_{NaP} Activation	
$m_\infty = 1/(1 + \exp[(V_m + 48.7)/(-4.4)])$	Fransén et al., (2004)
I_{NaP} Inactivation	
$\tau_h = 1/(\alpha + \beta)$	Magistretti and Alonso, (1999)
	Magistretti and Alonso, (1999)
$\alpha = \dfrac{-2.88 \cdot 10^{-3} V_m - 0.0491}{1 - \exp[(V_m + 17)/4.63]}$	
	Magistretti and Alonso, (1999)
$\beta = \dfrac{6.94 \cdot 10^{-3} V_m + 0.447}{1 - \exp[(V_m + 64.4)/(-2.63)]}$	
$h_\infty = 1/(1 + \exp[(V_m + 48.8)/9.98])$	Fransén et al., (2004)
Fast sodium I_{Na} activation	
$\tau_m = 1/(\alpha+\beta)$, $m_\infty = \alpha\tau$	Traub et al., (1991)
	Traub et al., (1991)
$\alpha = \dfrac{0.32(V_r - 13.1)}{1 - \exp[(V_r - 13.1)/(-4)]}$	
	Traub et al., (1991)
$\beta = \dfrac{-0.28(V_r - 40.1)}{1 - \exp[(V_r - 40.1)/5]}$	
$V_r = V_m + 54$	Traub et al., (1991)
Fast sodium I_{Na} inactivation	
$\tau_m = 1/(\alpha+\beta)$, $m_\infty = \alpha\tau$	Traub et al., (1991)
$\alpha = 0.128 \exp[(V_r - 17)/(-18)]$	Traub et al., (1991)
$\beta = 4/(1 + \exp[(V_r - 40)/(-5)])$	Traub et al., (1991)
$V_r = V_m + 54$	Traub et al., (1991)
Delayed rectifier I_K activation	
$\tau_m = 1/(\alpha + \beta)$, $m_\infty = \alpha\tau$	Traub et al., (1991)
	Traub et al., (1991)
$\alpha = \dfrac{0.016(V_r - 35.1)}{1 - \exp[(V_r - 35.1)/(-5)]}$	
$\beta = 0.25 \exp[(V_r - 20)/(-40)]$	Traub et al., (1991)
$V_r = V_m + 54$	Traub et al., (1991)

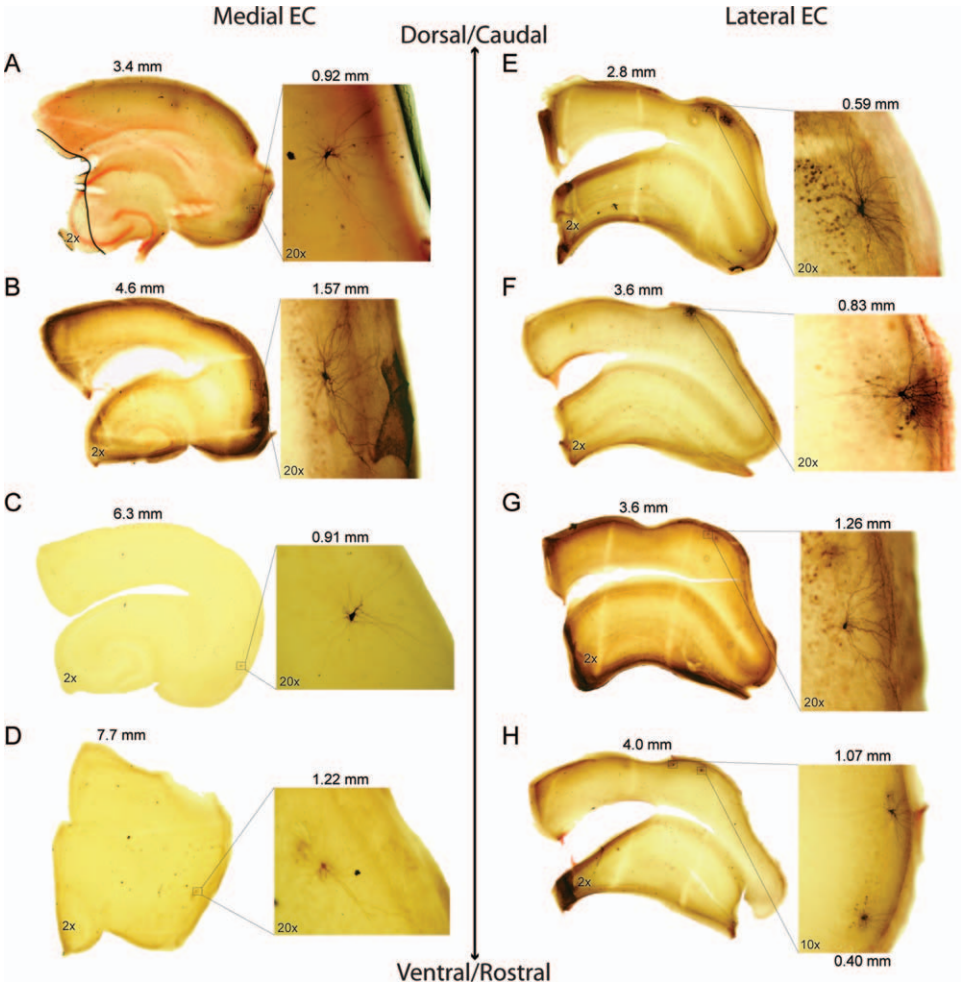

FIGURE 1. Anatomy and morphology in layer II cells of medial and lateral EC. (A–H) Panels in the left and right columns correspond to photomicrographs taken from medial EC in horizontal sections and lateral EC in coronal sections, respectively. In each panel, images on the left correspond to 2× magnification of the section to show the location of cells within each slice. Numbers correspond to the distance (mm) of each section from the dorsal (horizontal section, medial EC) or the caudal (coronal section, lateral EC) surface of the brain. Images on the right correspond to 20× (A–G) or 10× (H) magnification to show the detailed morphology of each cell. Numbers on right correspond to the distance (mm) of each cell from either the caudomedial tip of the horizontal slice (medial EC) or the center of the rhinal sulcus of the coronal slice (lateral EC). (A–D) Cells of the medial EC show radiating dendrites in all directions, indicative of stellate cells. (E–H) Cells of the lateral EC have dendrites that radiate horizontally across layer II and vertically into layer I, indicative of fan cells. [Color figure can be viewed in the online issue, which is available at wileyonlinelibrary.com.]

into layer I, resembling the morphology of fan cells (Tahvildari and Alonso, 2005). To better describe the coverage of medial and lateral EC, Figure 2 shows the estimated recording sites of medial (n = 53 out of 87) and lateral (n = 43 of 43) EC cells from horizontal and coronal sections, respectively. Our recording sites tended to stay within 2 mm of the caudomedial tip of the medial EC and within the dorsolateral band (close to the rhinal sulcus) of lateral EC.

Figure 3 shows the recordings of membrane potential from neurons in medial and lateral EC. Insets show a closer look at subthreshold voltage traces. In both medial and lateral EC, SMPOs appeared between the clusters of action potentials (Figs. 3A,D, asterisk). Subsequent current steps to the values beyond threshold increased the duration and the number of spikes within a cluster, generating a train of action potentials (Fig. 3A, arrowhead). Cluster firing was defined as in the previous studies (Klink and Alonso, 1993; Fransén et al., 2004) as cells displaying clear groups of spikes, often doublets or triplets, in which spiking events were separated by periods of subthreshold oscillations. There was a large difference between the responses of medial and lateral EC cells to nine successive 50 pA hyperpolarizing step currents. All medial EC cells showed large sag potentials in response to hyperpolarizing current steps (see Fig. 3B for individual traces and Fig. 3C for the mean sag across the population), whereas cells of lateral EC showed much smaller sag potentials at all hyperpolarization levels (Figs. 3E,F). Cells in medial EC showed rebound depolarization and spiking (Fig. 3B, asterisk) after hyperpolarizing current injection.

After examining cellular responses to depolarizing and hyperpolarizing current steps, ZAP stimuli were delivered at various

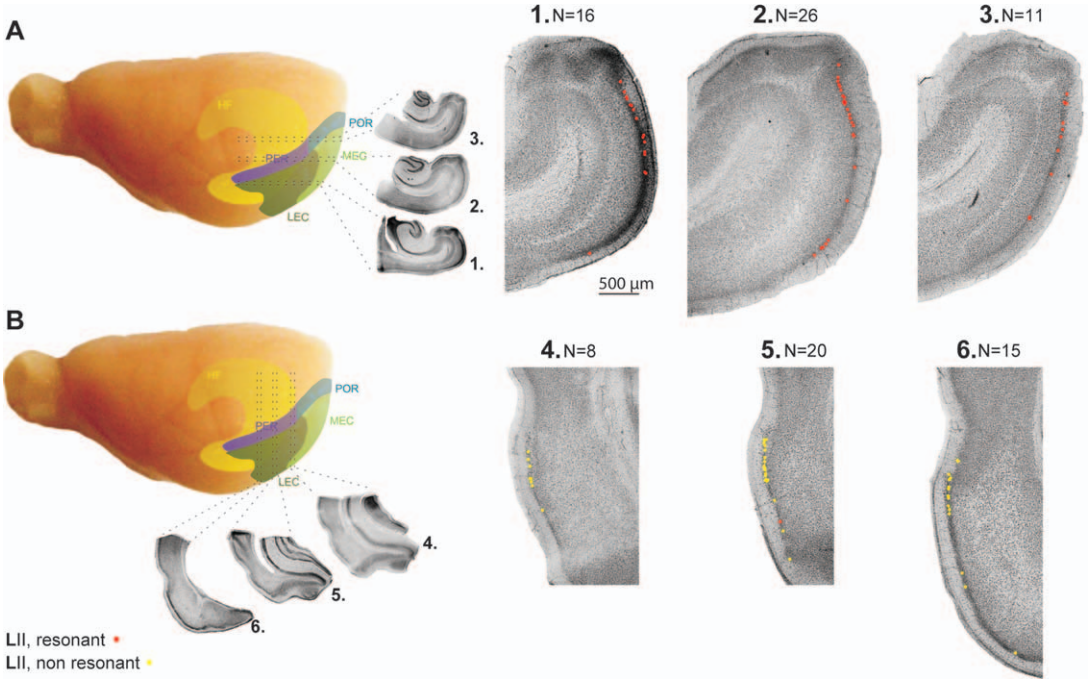

FIGURE 2. Slice orientation and anatomical location of recording sites in medial and lateral EC. (A,B) A whole brain schematic diagram depicting relative positions of the hippocampal formation and surrounding parahippocampal regions, as well as horizontal and coronal slice orientations. (1–3 left) Photomicrographs of representative whole slices taken along the *D*/*V* axis of medial EC from ventral (1, *n* = 16), intermediate (2, *n* = 26), and dorsal (3, *n* = 11) locations. (1–3 right) Higher power photomicrographs show the relative positions of recordings in medial EC layer II. *Note*: anatomical coordinates not available for every recorded cell (*n* = 53 cells mapped out of 87). (4–6 left) Photomicrographs of representative whole slices taken along the *M*/*L* axis of lateral EC from caudal (4, *n* = 8), intermediate (5, *n* = 20), and rostral (6, *n* = 15) locations. (4–6 right) Higher power photomicrographs show relative positions of recordings in lateral EC layer II (*n* = 43 out of 43). Red dots represent cells displaying resonance and yellow dots represent nonresonant cells. Abbreviations: HF, hippocampal formation (yellow); POR, postrhinal cortex (blue); PER, perirhinal cortex (purple); MEC, medial EC (light green); and LEC, lateral EC (dark green). Adapted with permission from Canto and Witter, 2011a,b, Copyright © 2011 WIley Periodicals, Inc.

membrane potentials to measure the resonant frequencies of each cell. Consistent with the previous studies, we found from these experiments that along the *D*/*V* axis of medial EC, cells showed a gradient in the resonant frequencies near resting potential such that higher frequencies were found in more dorsal regions and lower frequencies in more ventral regions. Figures 4A–F show the recordings with holding potentials of −65 mV from three medial and three lateral EC cells, respectively. In the medial EC, the resonant frequency decreased as a function of distance from the dorsal surface of the brain (A: 3.6 mm, 7.81 Hz; B: 5.0 mm, 6.16 Hz; and C: 6.7 mm, 3.97 Hz). However, in lateral EC, the resonant frequency was almost always under 2 Hz, regardless of the distance from the rhinal sulcus (coronal, D, 0.56 mm, 1.26 Hz; E, 0.92 mm, 0.88 Hz; and F, 1.81 mm, 0.76 Hz) or the dorsal surface of the brain (horizontal).

As ZAPs were delivered at different membrane potentials, the analyses of resonant frequency by *D*/*V* position were performed in 2-mV voltage bins according to the cell's membrane potential in each recording. Figures 5A–E show the plots of resonant frequency as a function of *D*/*V* position for five different voltage bins of medial EC cells as well as resultant r^2 values for linear fits to the data (A, −56.5 to −54.5 mV, r^2 = 0.00908; B, −60.5 to −58.5 mV, r^2 = 0.595; C, −62.5 to −60.5 mV, r^2 = 0.299; D, −64.5 to −62.5 mV, r^2 = 0.353; E, −70.5 to −68.5 mV, r^2 = 0.0246). At voltages near the resting membrane potential (Figs. 5B–D), the resonant frequency clearly decreased along the *D*/*V* axis in the medial EC. However, at membrane potentials away from rest, slopes flattened out, suggesting that the relationship between resonant frequency and membrane potential is weaker at these voltages. Unlike medial EC cells, Figures 5F–O show that the lateral EC cells lacked resonant properties, regardless of their anatomical position in both horizontal (Figs. 5F–J) and coronal (Figs. 5K–O) sections.

An important result from the ZAP analyses was the inverse linear relationship found between membrane potential and resonant frequency in all cells of the medial EC. Figures 6A–C show that as the membrane potential becomes more depolarized the resonant frequency decreases, or stated another way, as the membrane potential becomes more hyperpolarized, the resonant frequency increases (A: −62 mV, 3.38 Hz; B: −67 mV, 4.79 Hz; and C: −72 mV, 6.04 Hz). The linear relationship between resonant frequency and membrane potential from −70 to −55 mV can be found in the plots for three individual medial entorhinal neurons in dorsal medial regions

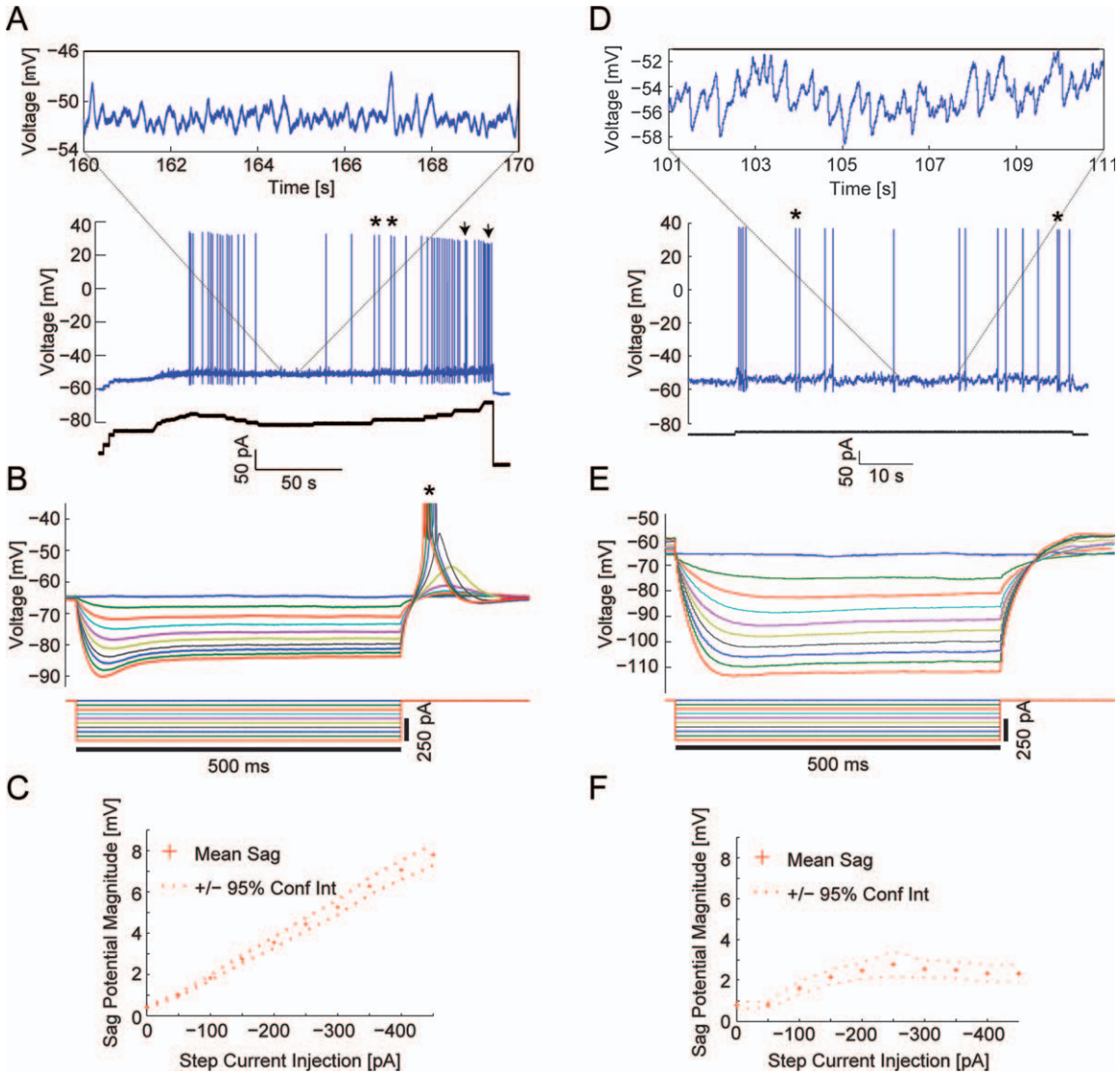

FIGURE 3. Physiological properties differ between cells of medial and lateral EC. (A–F) Panels in the left and right columns correspond to data from a single cell in medial EC and lateral EC (coronal), respectively. (A) As the holding current is gradually increased, medial EC cells display spike clustering near threshold (asterisks) that turns into trains of spikes (arrowheads) at more suprathreshold membrane potentials. In between clusters, medial EC cells display subthreshold oscillations (inset). (D) Overall, cells of the lateral EC (coronal and horizontal sections) were very excitable, requiring smaller input currents (bottom of panels A and D) to elicit spiking compared to cells of the medial EC. The inset shows the presence of oscillations in one example cell in lateral EC. (B,E) In response to nine successive −50 pA current steps, sag potentials, likely dependent on I_h, are displayed in cells of medial EC (B) but not lateral EC (E). Often, medial EC cells displayed rebound spikes following the release from the step current. (B) These rebound spikes (asterisk) are truncated to enhance visualization of the sag potentials. (C,F) Among all cells recorded, the mean sag potential across all hyperpolarizing steps was nearly fourfold larger for medial EC cells (C, $n = 65$) compared to lateral EC cells recorded from coronal sections (F, $n = 43$). [Color figure can be viewed in the online issue, which is available at wileyonlinelibrary.com.]

in Figure 6G and in ventral medial regions in Figure 6H. The linear relationship in this membrane potential range was found in every cell of the medial EC (see later figures). In contrast, in the lateral EC, almost all cells showed resonant frequencies of <2 Hz across all membrane potentials. Three examples of this are shown in Figures 6D–F. Only a few cells in lateral EC showed resonant frequencies above 2 Hz, and those that did had frequencies that were always below 3 Hz. Examples of the resonant frequency at different membrane potentials in individual dorsal and ventral lateral EC neurons are shown in Figures 6I,J.

We simulated the inverse linear relationship between membrane potential and resonant frequency by constructing a biophysical model of layer II medial EC stellate cells. We performed simulations with various holding currents to systematically test the effect of mean membrane potential on the resonant frequency. In Figures 7A–D, example voltage and impedance traces are shown for four mean membrane potentials,

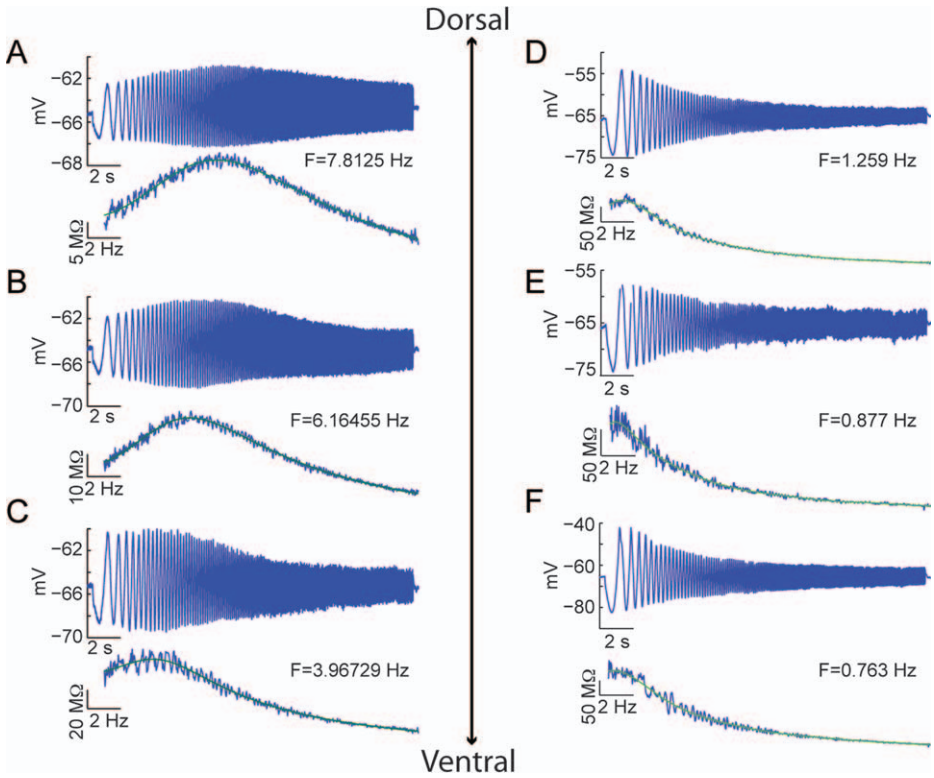

FIGURE 4. Resonant frequency decreases along the *D*/*V* axis of medial EC. (A–F) ZAP stimuli (input not shown) were set to appropriate amplitudes that ensured subthreshold membrane potential dynamics. For each recording, the cell's membrane potential response is on top, and below is the cell's impedance as well as the impedance curve fit to estimate the cell's resonant frequency from the peak of the curve. In these figures, each cell was held with a holding current to a mean membrane potential of −65 mV. (A–C) Example recordings from medial EC cells at three different *D*/*V* depths (A, 3.6 mm; B, 5.0 mm; and C, 6.7 mm from the dorsal surface). The resonant frequency decreases as a function of distance from the dorsal surface of the brain. (D–F) Example recordings from lateral EC cells (coronal sections) at three different *D*/*V* depths (D, 0.555 mm; E, 0.919 mm; and F, 1.812 mm from the rhinal sulcus). Unlike medial EC, cells in lateral EC have resonant frequencies below 2 Hz, regardless of their *M*/*L* position.[Color figure can be viewed in the online issue, which is available at wileyonlinelibrary.com.]

whereas Figure 7E shows the voltage dependence of the *H*-current channel activation, inverse time constant, and the resonant frequency. At more hyperpolarized membrane potentials, the *H*-current activation and inverse time constant are large, leading to higher resonant frequencies. As the model cell becomes more depolarized, activation of the *H*-current and its inverse time constant decrease, resulting in lower resonant frequencies. It is important to note that at membrane potentials between −55 and −70 mV the simulations gave an approximately linear relationship with a negative slope. This result is in agreement with what was found experimentally. At more hyperpolarized membrane potentials (−70 to −85 mV) tested in the biophysical model, the activation of the *H*-current approaches its maximum, causing the resonant frequency to approach an asymptotic level.

We then checked to see if this same phenomenon of approach to an asymptotic level occurred in vitro, by measuring the resonant frequency at more hyperpolarized levels (−55 to −80 mV, $n = 17$) and (−60 to −90 mV, $n = 7$) in layer II medial EC cells. The results of these experiments (Figs. 8A–F,I) show that at membrane potentials below −70 mV, the resonant frequency approaches an asymptotic value, suggesting saturation to a maximum resonant frequency. Figure 8 also highlights some other important findings of this study. Controls recorded at different time points 10 min apart show that the resonant frequency was very stable (Figs. 8A,B) and we found that the resonant frequency does not show hysteresis (Figs. 8C–F). We measured the voltage dependence of resonance in four different ways. First, as was performed for all other cells, the resonant frequency was measured from hyperpolarized to depolarized membrane potentials. This was usually done without returning the membrane potential to rest between individual holding potentials. However, in cells shown in Figures 8C,D, we stepped to rest before each step in the depolarized direction. We also reversed the voltage direction in which we measured the resonant frequency, so as to start at −55 mV and end at −80 mV. Additionally, we measured the resonant frequency at randomly chosen voltages. In all cases ($n = 14$ cells), the voltage direction did not appreciably alter the voltage dependence of the resonant frequency. To ensure that our results were not influenced by the use of different amplitudes of the ZAP stimulus, we held medial EC cells ($n = 6$) at three different potentials (−65, −70, and −75 mV) and measured the resonant frequency with 40, 80, 120, and 200 pA peak-to-

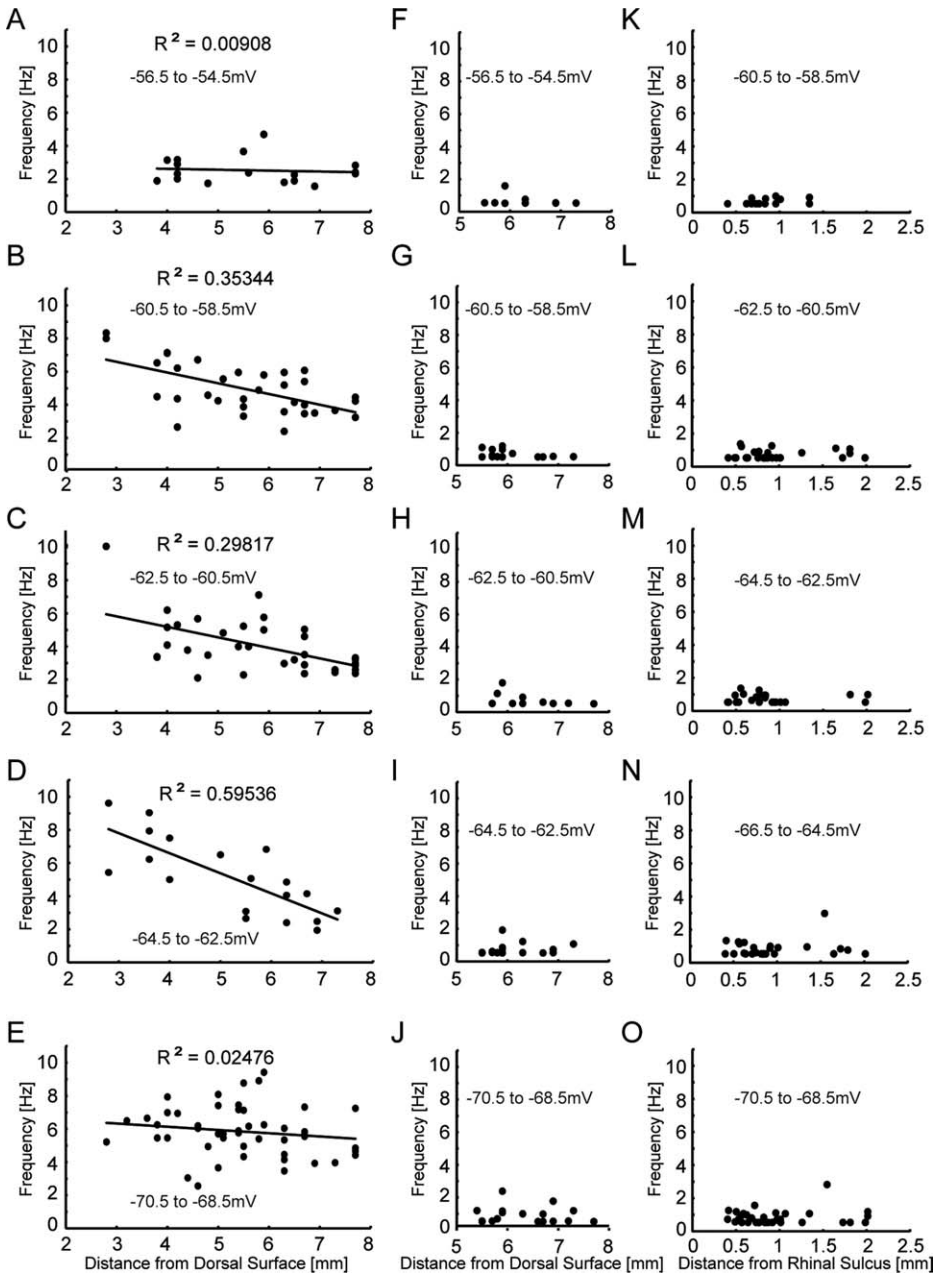

FIGURE 5. The medial EC population shows a clear decrease of the resonant frequency along the *D*/*V* axis at membrane potentials near resting potential. (A–J) Resonant frequencies, recorded from horizontal sections, are plotted as a function of *D*/*V* distance according to 2-mV membrane potential bins (A, F, −56.5 to −54.5 mV; B, G, −60.5 to −58.5 mV; C, H, −62.5 to −60.5 mV; D, I, −64.5 to −62.5 mV; and E, J, −70.5 to −68.5 mV). (A–E) In the membrane potential bins near rest (B–D), the resonant frequency in medial EC cells decreased with increasing distance from the dorsal surface. However, at membrane potentials away from rest the slopes flattened out (A,E). (F–J) Independent of membrane potential and position along the *D*/*V* axis, lateral EC cells rarely have resonant frequencies above 2 Hz. (K–O) Similar to the recordings in horizontal sections, lateral EC cells recorded from coronal sections rarely have resonant frequencies above 2 Hz, regardless of *D*/*V* position or membrane potential (K, −60.5 to −58.5 mV; L, −62.5 to −60.5 mV; M, −64.5 to −62.5 mV; N, −66.5 to −64.5 mV; O, −70.5 to −68.5 mV).

peak amplitude ZAP stimuli at each potential. In all six cells, we found that the resonant frequency was very similar at a given potential, regardless of the ZAP amplitude used. Examples from two cells are shown in Figures 8G,H. The correlation between the presence of the *H*-current and the resonant properties prompted experiments where the *H*-current blocker, ZD7288, was applied to medial EC cells. These experiments abolished both the sag potential (data not shown) and the resonant properties (Figs. 9A–C, $n = 3$) in medial EC cells. In addition, the firing properties of the medial EC cells became very similar to those in the lateral EC, and stopped showing firing of spikes in clusters.

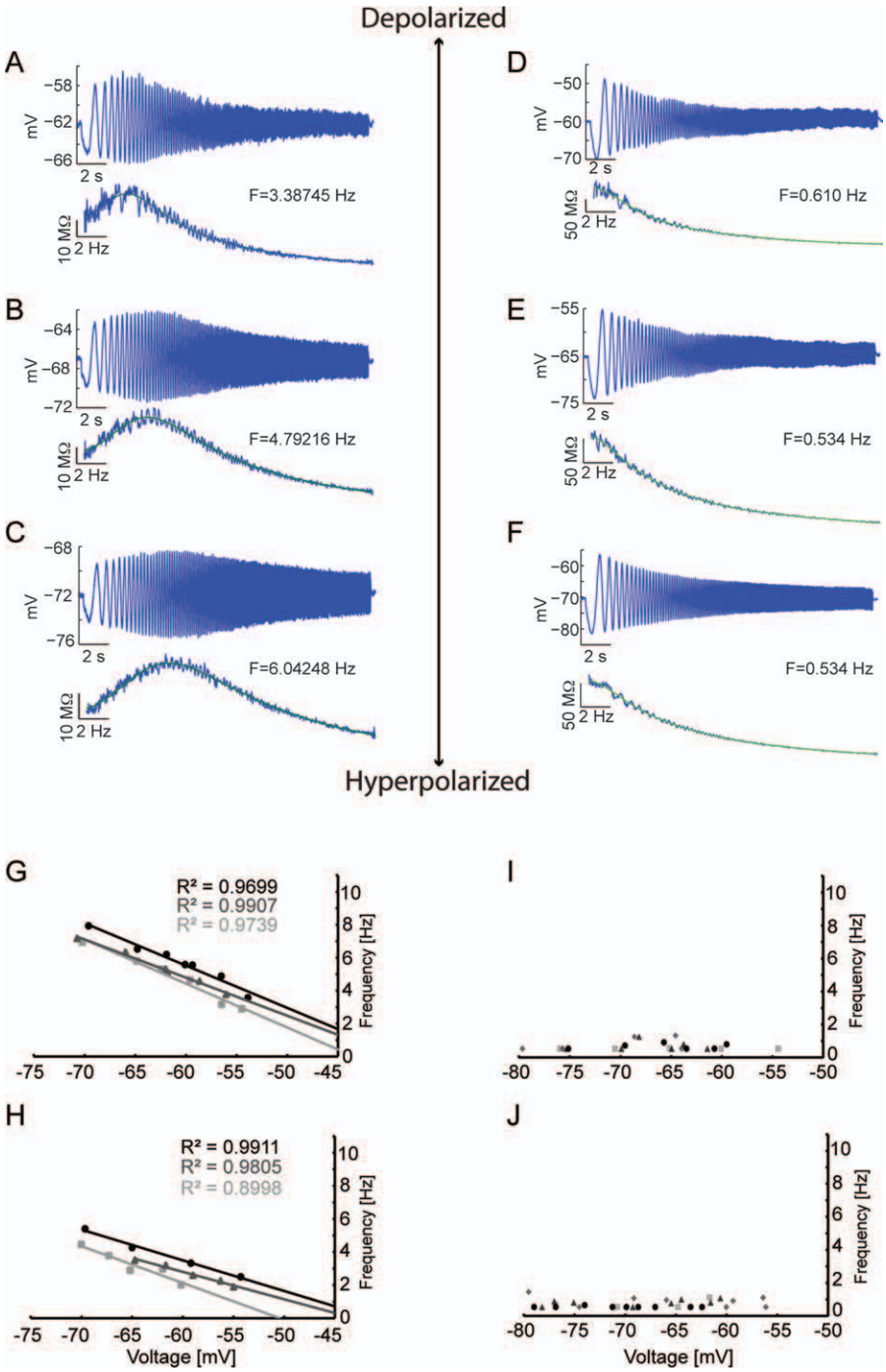

FIGURE 6. Resonant frequency decreases with membrane potential depolarization in medial EC. (A–F) ZAP stimuli were set to appropriate amplitudes that ensured subthreshold membrane potential dynamics. For each recording, the cell's membrane potential response is on top, and below is the cell's impedance as well as the impedance curve fit to estimate the cell's resonant frequency from the peak of the curve. (A–C) The membrane potential dependence of the resonant frequency is exemplified in three recordings from a single cell in medial EC, 3.8 mm from the dorsal surface of the brain. At membrane potentials of −62 mV (A), −67 mV (B), and −72 mV (C), the resonant frequencies were 3.39, 4.79, and 6.04 Hz, respectively. (D–F) In contrast, three recordings from a lateral EC cell (coronal section) show that at −60 mV (D), −65 mV (E), and −70 mV (F), the resonant frequency is below 2 Hz. (G,H) Plots of resonant frequency versus membrane potential are shown for three individual cells in dorsal medial EC (G, circle, 4 mm; triangle, 3.8 mm; and square, 4.2 mm from dorsal surface) and ventral medial EC (H, circle, 5.8 mm; triangle, 6.5 mm; and square, 6.3 mm from dorsal surface). In cells of the medial EC (G,H), there is an inverse linear relationship between membrane potential and resonant frequency. (I,J) In contrast, lateral EC cells lack resonant properties in both dorsal (I, circle, 1.010 mm; triangle, 0.834 mm; square, 0.621 mm; and diamond. 0.415 mm from the rhinal sulcus) and ventral lateral EC (J, circle, 1.986 mm; triangle, 1.812 mm; square, 1.651 mm; and diamond, 1.344 mm from the rhinal sulcus). Cells in dorsal medial EC (G) have higher resonant frequencies than in ventral medial EC (H). [Color figure can be viewed in the online issue, which is available at wileyonlinelibrary.com.]

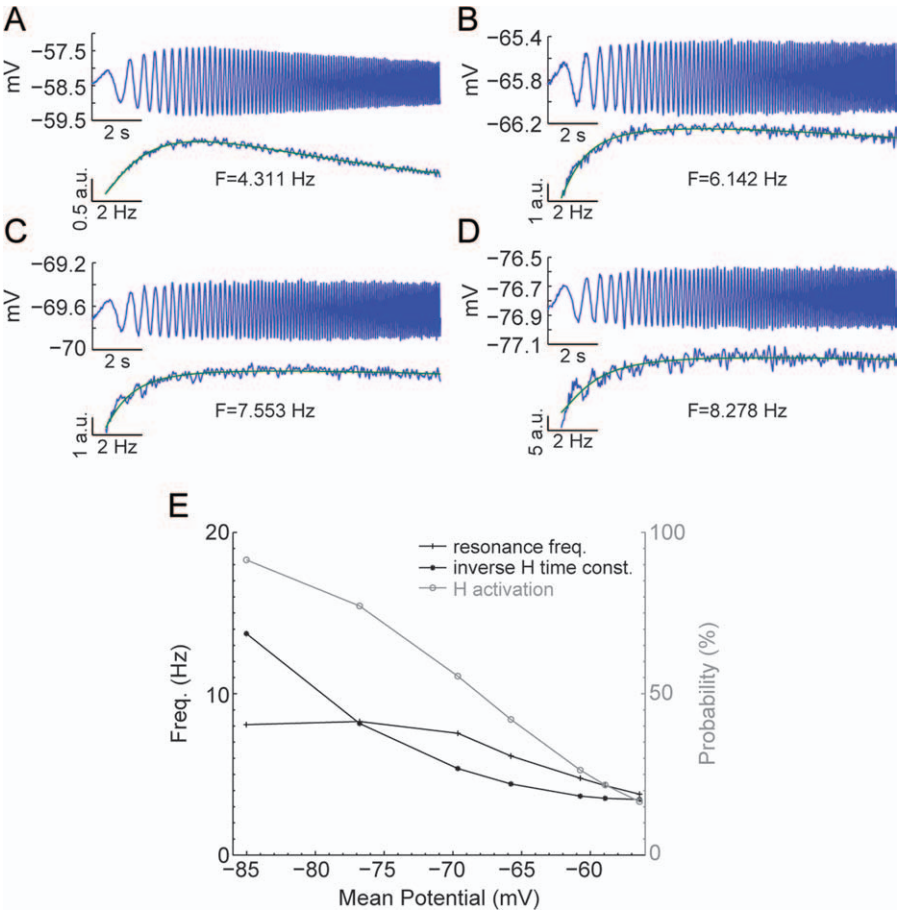

FIGURE 7. Biophysical model of medial EC cells displays relationship between increase in membrane potential and decrease in resonant frequency. (A–D) Simulated membrane potential trace (top), impedance, and impedance curve fits (bottom) at four different membrane potentials (A, −58.5 mV; B, −65.8 mV; C, −69.6 mV; and D, −76.8 mV). At depolarized membrane potentials close to threshold, the resonant frequency is decreased compared to the more hyperpolarized membrane potentials. (E) Summary plot of biophysical simulations shows that as membrane potential is hyperpolarized, the resonant frequency increases linearly until saturation occurs with approach to an asymptotic frequency between −70 and −85 mV. The inverse *H*-current time constant and activation both increase as the membrane potential is hyperpolarized, contributing to the increase in frequency with hyperpolarization. Abbreviations: a.u., arbitrary units. [Color figure can be viewed in the online issue, which is available at wileyonlinelibrary.com.]

We then pooled the medial EC data measuring the resonant frequency from −55 to −70 mV and from −55 to −80 mV. The finding of higher resonant frequencies in dorsal medial EC compared to ventral medial EC still held true (Figs. 10A,B). In addition, across the population the dorsal cells showed more of an asymptotic approach to a maximum across membrane potentials compared to the ventral population. Finally, we investigated how the slope of resonance versus membrane potential (Hz/mV) changes for individual cells along the *D*/*V* axis of the medial EC. For all cells ($n = 87$), we looked at the slope of resonant frequency versus membrane potential computed across the full range of membrane potentials from −80 to −55 mV (Fig. 10C) and a more limited range from −70 to −55 mV (Fig. 10D). In both analyses, the difference in slope of resonance frequency versus membrane potential showed an apparent negative trend along the *D*/*V* axis, but this trend did not reach statistical significance (Figs. 10C,D).

DISCUSSION

The physiological results presented here show a systematic difference in resonance frequency with mean membrane potential in neurons of the medial EC. This can be described as an increase in resonance frequency with hyperpolarization or a decrease in resonance frequency with depolarization. This change in resonance frequency with mean membrane potential appears to be linear in the range from −70 to −55 mV, and shows an asymptotic approach to a maximum frequency at more hyperpolarized levels. The change in resonance frequency was tested at anatomical positions along the *D*/*V* axis of medial EC. Consistent with the previous studies (Giocomo et al., 2007; Giocomo and Hasselmo, 2008a,b; Giocomo and Hasselmo, 2009; Boehlen et al., 2010), the resonance frequency shows a gradient from higher frequencies in dorsal neurons to lower frequencies in ventral neurons, but this gradient primarily

appears at membrane potentials around resting potential. The gradient does not appear at more hyperpolarized membrane potentials, potentially owing to the asymptotic approach to a limiting frequency at more hyperpolarized membrane potentials, as demonstrated in both the experimental data and the biophysical simulation. The asymptotic approach to a limiting frequency was suggested by the previous data showing similar resonance frequencies at −70 and −80 mV (Nolan et al., 2007).

A recent study reported that as animals mature, cells in the dorsal medial EC change their frequency preference twofold, whereas the preference of ventral cells remains relatively unchanged (Boehlan et al., 2010). As we used animals at ages (p 17–21) where the network is still developing, cells in dorsal medial EC would be expected to have greater variability in their resonant frequencies compared to ventral cells. The combined factors of increased variability and the asymptotic approach to a limiting frequency could be the reasons why the systematic decrease in resonance frequency along the *D*/*V* axis was obfuscated at membrane potentials away from rest. The age of the animals did not affect the linear relationship between membrane potential voltage and resonant frequency as every resonant cell showed this relationship, regardless of the age of the animal.

The data also show a clear difference in resonance properties of medial versus lateral EC that further supports the proposal that intrinsic resonance properties of entorhinal neurons contribute to the spatial periodicity of grid cells, as the distribution of resonance in medial but not lateral EC shown here is consistent with the appearance of grid cells in medial EC (Fyhn et al., 2004; Hafting et al., 2005; Hafting et al., 2008) and the relative absence of spatial information in the response of neurons in the lateral EC (Hargreaves et al., 2005; Yoganarasimha et al., 2011). Our data showing the relative absence of resonance properties in lateral EC are also consistent with the smaller amplitude of theta rhythm oscillations observed in lateral versus medial EC (Deshmukh et al., 2010) and the previous observations on lesser MPOs in lateral EC (Tahvildari and Alonso, 2005). It should be noted, however, that given that the majority of our lateral EC data were recorded from the dorsolateral band, lateral EC cells in more intermediate and ventral positions could possibly possess resonance and oscillation properties. This could function as a possible mechanism to aid frequency-dependent information flow between the medial EC and the lateral EC. Anatomical studies have shown that synaptic contacts between medial and lateral EC are limited, but indeed present (Dolorfo and Amaral, 1998; Rowland et al., 2011).

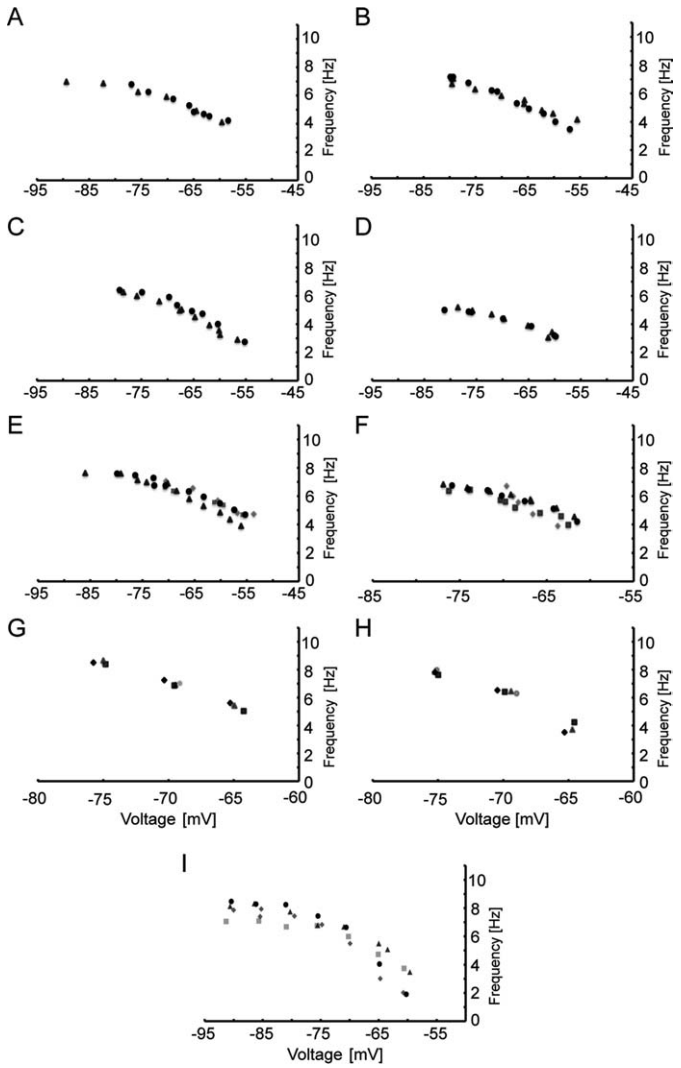

FIGURE 8.

FIGURE 8. The resonant frequency in medial EC approaches an asymptotic value at membrane potentials below −70 mV, does not display hysteresis, and is not affected by the amplitude of the ZAP stimulus. (A,B) The resonant frequency shown at more hyperpolarized potentials (−80 to −55 mV, circles) in two different cells. After 10 min, resonance frequency was measured again (triangles) to test the stability of the resonant frequency. Both example cells show no appreciable difference at different times. (C,D) The resonance frequency was measured from −80 to −55 mV (circles) and then remeasured with steps to rest before each step to a more depolarized potential (triangles). (E,F) The resonant frequency was initially measured sequentially from −55 to −80 mV (circles), and then the order of membrane potentials was switched to start at −80 and end at −55 mV (triangles). Next, random membrane potentials were chosen to measure the resonant frequency (squares). Finally, the direction returned to that used initially, −55 to −80 mV (diamonds). In each case, cells did not exhibit hysteresis. All cells showed a linear relationship between the membrane potential and the resonant frequency between −55 and −70 mV that then approached an asymptote at more hyperpolarized membrane potentials. (G,H) The resonant frequency was measured at −65, −70, and −75 mV using 40 pA (diamonds), 80 pA (squares), 120 pA (triangles), and 200 pA (circles) peak-to-peak ZAP amplitude stimuli (n = 6). Examples from single cells are shown (G,H). In all cases, the resonant frequency was very similar at a given potential for all ZAP amplitudes tested. (I) To highlight the asymptotic behavior of the resonant frequency, four examples (n = 7) are shown with membrane potentials ranging from −60 to about −90 mV. Cells were located at 3.8 mm (squares), 4.6 mm (triangles and diamonds), and 5.0 mm (circles) from the dorsal surface.

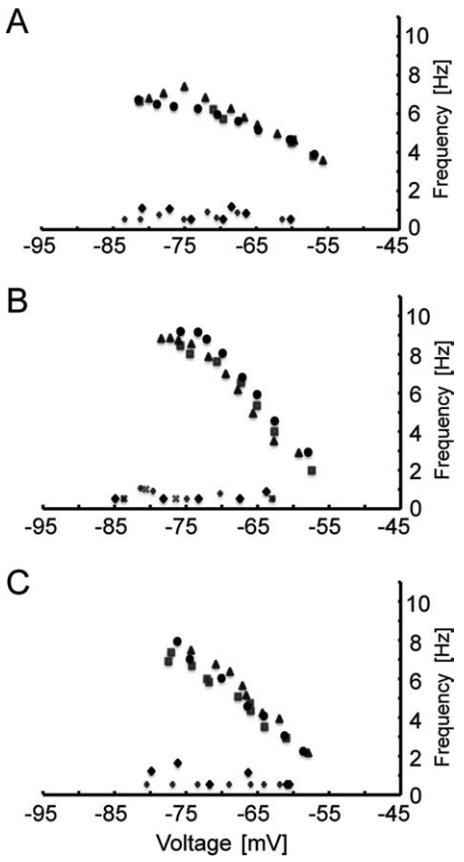

FIGURE 9. ZD7288 abolishes resonance properties in medial EC. (A–C) The resonant frequency was measured in three membrane potential directions (A, B: −55 to −80 mV, circles; −80 to −55 mV, triangles; random membrane potentials, squares, and C: −80 to −55 mV, circles; −55 to −80 mV, triangles, and random membrane potentials, squares) before continuously washing 10 μM ZD7288 into the bath. The resonant frequency was then measured after 10 min in ZD7288 in both directions as before. Cell (C) was also tested using the ZAP stimulus at random mean membrane potentials. In all cases, the ZD7288 abolished the resonant frequency at all mean membrane potentials tested.

The anatomical distribution of resonance properties is consistent with oscillatory interference models that link intrinsic frequencies and the generation of grid cells (Burgess et al., 2007; Hasselmo et al., 2007). Similarly, the important role of head direction input for grid cell generation in oscillatory interference models (Burgess et al., 2007; Hasselmo et al., 2007) and attractor models (Fuhs and Touretzky, 2006; McNaughton et al., 2006; Gaussier et al., 2007; Guanella et al., 2007; Burak and Fiete, 2009) is also consistent with the selective anatomical input from the dorsal presubiculum to the medial but not the lateral EC (Witter et al., 1989; Witter and Moser, 2006). The dorsal presubiculum (postsubiculum) providing this input shows strong head direction response properties (Taube et al., 1990; Taube and Bassett, 2003; Brandon et al., 2011a) as well as intrinsic properties that could assist in persistence of head direction coding (Yoshida and Hasselmo, 2009).

How does resonance underlie the spatial periodicity of grid cells? Early models focused on the fact that the same intrinsic properties that generate resonance also generate MPOs, and used oscillatory interference between MPOs within single neurons. But as described in the Introduction section, models using MPOs have problems with the variance of MPO periods (Welinder et al., 2008; Giocomo and Hasselmo, 2008a; Zilli et al., 2009), with the synchronization properties of MPOs (Remme et al., 2009), and with the lack of linear changes in MPO frequency with membrane potential (Yoshida et al., 2011), though it is possible that high density of *H*-current in distal dendrites allows more local interference interactions (Magee, 1998).

As an alternative, our data show that the resonance properties of neurons provide an intrinsic frequency that changes in a linear manner for membrane potentials between −70 and −55 mV. This resonance may contribute to local circuit oscillations involving interactions of populations of excitatory cells, or interactions of excitatory cells with inhibitory cells (Zilli and Hasselmo, 2010). Neurons responsive to running speed (Sharp, 1996; O'Keefe et al., 1998) and head direction (Taube et al., 1990; Taube and Bassett, 2003; Sargolini et al., 2006) might depolarize membrane potential and thereby shift the frequency of local circuit interactions that generate grid cell periodicity. Note that the oscillatory interference models of grid cells work just as well with both a positive and a negative slope of frequency to velocity (Giocomo and Hasselmo, 2008a), as long as the difference in frequencies shows a linear relationship with running velocity. A linear relationship between resonance frequency and depolarization appears between −70 and −55 mV in the data presented here. This means that the difference in resonant frequency between neurons would change linearly with changes in membrane potential in this range. In fact, the nonlinear relationship of frequency to membrane potential found when extending to membrane potentials below −70 mV in the data presented here could be compensated by a nonlinear change in input with velocity (Zilli and Hasselmo, 2010).

The resonance properties of excitatory cells might interact with a theta rhythmic input to interneurons in the EC from the medial septum (Alonso and Kohler, 1984). This is consistent with the recent data showing that reduction of theta rhythm oscillations in the EC by pharmacological inactivation of the medial septum is associated with a loss of spatial periodicity in grid cells (Brandon et al., 2011b; Koenig et al., 2011), but with maintenance of head direction responses (Brandon et al., 2011b) and place cell responses (Koenig et al., 2011). Interactions of the resonance frequency with a network theta rhythm oscillation could also underlie the phenomenon of theta cycle skipping that appears in the many medial entorhinal neurons (Deshmukh et al., 2010), and is reduced during infusions of muscimol into the medial septum (Brandon et al., 2011b).

The data do not show a significant difference in slope of resonance frequency to membrane potential at different *D*/*V* positions. A difference in slope would be interesting as differences in the properties of resonance frequency at different *D*/*V* positions (Giocomo et al., 2007; Boehlen et al., 2010) could underlie the difference in both spacing and size of grid cell

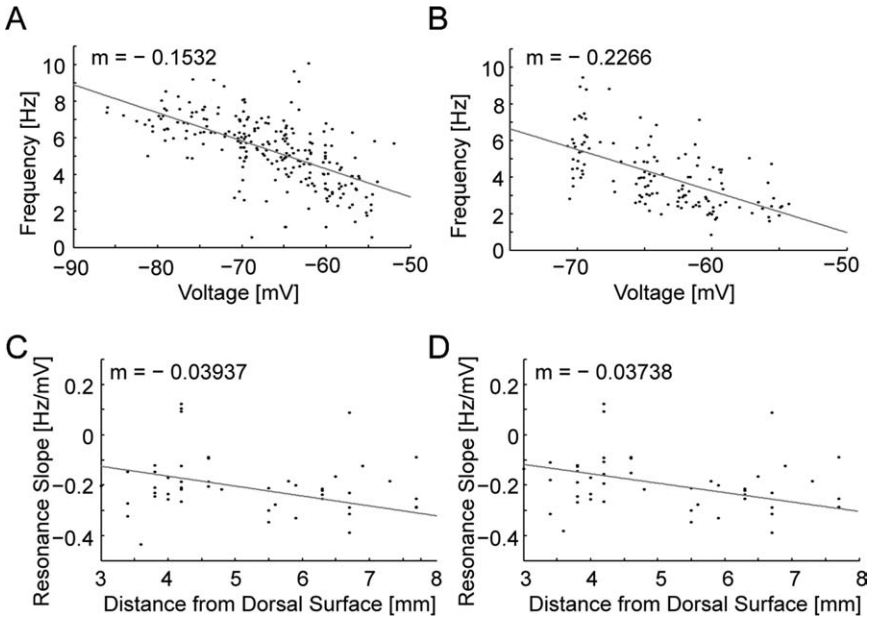

FIGURE 10. Population data showing resonant frequencies at all membrane potentials in dorsal medial EC compared to ventral EC. (A,B) Cells in the dorsal medial EC (A, $n = 48$) show higher frequencies compared to ventral medial EC cells (B, $n = 31$) and a clearer approach to an asymptotic frequency. (C,D) The slope of resonant frequency as a function of membrane potential is plotted for individual cells based on their distance from the dorsal surface. The slope of resonant frequencies against membrane potential was calculated for the full data from −55 to −80 mV (C) or for a smaller range from −55 to −70 mV (D), showing no significant difference along the *D*/*V* axis of the EC.

firing fields along the *D*/*V* axis. The change in spacing and size of grid cell firing fields observed in association with the novelty of environments (Barry et al., 2008) could arise from novelty-induced changes in acetylcholine levels in cortical structures (Acquas et al., 1996) that activate muscarinic receptors to change the resonance frequency of stellate cells in medial EC (Heys et al., 2010).

In the oscillatory interference models, the lack of resonance properties in lateral entorhinal neurons would result in a lack of spatial periodicity of these neuron responses. The oscillatory interference models provide a clear link between the intrinsic properties of neurons and the functional grid cell firing properties, including properties of theta phase precession by grid cells (Burgess, 2008; Hafting et al., 2008) and the dependence of intrinsic frequency of grid cells on running speed and size of grid fields (Jeewajee et al., 2008). This link is less apparent in other models of grid cells, such as the attractor dynamic models that depend on patterns of synaptic connectivity rather than the intrinsic properties of neurons (Fuhs and Touretzky, 2006; McNaughton et al., 2006; Burak and Fiete, 2009). However, recent models combine attractor dynamics with intrinsic properties such as the medium AHP (Storm, 1989) to account for features of grid cells such as theta phase precession (Navratilova et al., 2011). Another type of model uses intrinsic properties to generate grid cell responses via self-organization of afferent input (Kropff and Treves, 2008).

The nonspatial properties of lateral entorhinal neurons has led to proposals that they play a role in the coding of objects or items to be associated with the spatial or temporal context coded by medial EC (Hargreaves et al., 2005; Witter and Moser, 2006; Eichenbaum and Lipton, 2008). In this framework, a spatiotemporal trajectory may be encoded by interactions of the medial EC and hippocampus, and associations with events or items at specific spatiotemporal positions along the trajectory could involve interactions of neurons in the medial EC coding space and time with neurons in the lateral EC coding items and objects associated with specific events (Hasselmo, 2009).

REFERENCES

Acquas E, Wilson C, Fibiger HC. 1996. Conditioned and unconditioned stimuli increase frontal cortical and hippocampal acetylcholine release: effects of novelty, habituation, and fear. J Neurosci 16:3089–3096.

Alonso A, Klink R. 1993. Differential electroresponsiveness of stellate and pyramidal-like cells of medial entorhinal cortex layer II. J Neurophysiol 70:128–143.

Alonso A, Kohler C. 1984. A study of the reciprocal connections between the septum and the entorhinal area using anterograde and retrograde axonal transport methods in the rat brain. J Comp Neurol 225:327–343.

Alonso A, Llinas RR. 1989. Subthreshold Na-dependent theta-like rhythmicity in stellate cells of entorhinal cortex layer II. Nature 342:175–177.

Barry C, Fleming SM, Jeewajee A, O'Keefe J, Burgess N. 2008. Effect of novelty on grid cell firing. Proc ICCNS 12:35.

Blair HT, Welday AC, Zhang K. 2007. Scale-invariant memory representations emerge from moire interference between grid fields that produce theta oscillations: a computational model. J Neurosci 27:3211–3229.

Blair HT, Gupta K, Zhang K. 2008. Conversion of a phase- to a rate-coded position signal by a three-stage model of theta cells, grid cells, and place cells. Hippocampus 18:1239–1255.

Boehlen A, Heinemann U, Erchova I. 2010. The range of intrinsic frequencies represented by medial entorhinal cortex stellate cells extends with age. J Neurosci 30:4585–4589.

Brandon MP, Bogaard A, Andrews C, Hasselmo ME. 2011a. Head direction cells in the postsubiculum do not show replay of prior waking sequences during sleep. Hippocampus (in press).

Brandon MP, Bogaard AR, Libby CP, Connerney MA, Gupta K, Hasselmo ME. 2011b. Reduction of theta rhythm dissociates grid cell spatial periodicity from directional tuning. Science 332:595–599.

Burak Y, Fiete IR. 2009. Accurate path integration in continuous attractor network models of grid cells. PLoS Comput Biol 5:e1000291.

Burgess N. 2008. Grid cells and theta as oscillatory interference: theory and predictions. Hippocampus 18:1157–1174.

Burgess N, Barry C, Jeffery KJ, O'Keefe J. 2005. A grid and place cell model of path integration utilizing phase precession versus theta. Computational Cognitive Neuroscience Meeting, Washington, DC.

Burgess N, Barry C, O'Keefe J. 2007. An oscillatory interference model of grid cell firing. Hippocampus 17:801–812.

Canto CB, Witter MP. 2011a. Cellular properties of principal neurons in the rat enthorinal cortex. I. The lateral entorhinal cortex. Hippocampus (in press).

Canto CB, Witter MP. 2011b. Cellular properties of principal neurons in the rat entorhinal cortex. II. The medial entorhinal cortex. Hippocampus (in press).

Deshmukh SS, Yoganarasimha D, Voicu H, Knierim JJ. 2010. Theta modulation in the medial and the lateral entorhinal cortices. J Neurophysiol 104:994–1006.

Dickson CT, Magistretti J, Shalinsky MH, Fransén E, Hasselmo ME, Alonso A. 2000. Properties and role of I(h) in the pacing of subthreshold oscillations in entorhinal cortex layer II neurons. J Neurophysiol 83:2562–2579.

Dodson PD, Pastoll H, Nolan MF. 2011. Dorsal-ventral organization of theta-like activity intrinsic to entorhinal stellate neurons is mediated by differences in stochastic current fluctuations. J Physiol 589(Part 12):2993–3008.

Dolorfo CL, Amaral DG. 1998. Entorhinal cortex of the rat: organization of intrinsic connections. J Comp Neurol 398:49–82.

Eichenbaum H, Lipton PA. 2008. Towards a functional organization of the medial temporal lobe memory system: role of the parahippocampal and medial entorhinal cortical areas. Hippocampus 18:1314–1324.

Erchova I, Kreck G, Heinemann U, Herz AV. 2004. Dynamics of rat entorhinal cortex layer II and III cells: characteristics of membrane potential resonance at rest predict oscillation properties near threshold. J Physiol 560 (Part 1):89–110.

Fransén E, Alonso AA, Dickson CT, Magistretti J, Hasselmo ME. 2004. Ionic mechanisms in the generation of subthreshold oscillations and action potential clustering in entorhinal layer II stellate neurons. Hippocampus 14:368–384.

Fuhs MC, Touretzky DS. 2006. A spin glass model of path integration in rat medial entorhinal cortex. J Neurosci 26:4266–4276.

Fyhn M, Molden S, Witter MP, Moser EI, Moser MB. 2004. Spatial representation in the entorhinal cortex. Science 305:1258–1264.

Gaussier P, Banquet JP, Sargolini F, Giovannangeli C, Save E, Poucet E. 2007. A model of grid cells involving extra hippocampal path integration, and the hippocampal loop. J Integr Neurosci 6:447–476.

Giocomo LM, Hasselmo ME. 2008a. Computation by oscillations: implications of experimental data for theoretical models of grid cells. Hippocampus 18:1186–1199.

Giocomo LM, Hasselmo ME. 2008b. Time constants of h current in layer II stellate cells differ along the dorsal to ventral axis of medial entorhinal cortex. J Neurosci 28:9414–9425.

Giocomo LM, Hasselmo ME. 2009. Knock-out of HCN1 subunit flattens dorsal-ventral frequency gradient of medial entorhinal neurons in adult mice. J Neurosci 29:7625–7630.

Giocomo LM, Zilli EA, Fransén E, Hasselmo ME. 2007. Temporal frequency of subthreshold oscillations scales with entorhinal grid cell field spacing. Science 315:1719–1722.

Guanella A, Kiper D, Verschure P. 2007. A model of grid cells based on a twisted torus topology. Int J Neural Syst 17:231–240.

Haas JS, White JA. 2002. Frequency selectivity of layer II stellate cells in the medial entorhinal cortex. J Neurophysiol 88:2422–2429.

Hafting T, Fyhn M, Molden S, Moser MB, Moser EI. 2005. Microstructure of a spatial map in the entorhinal cortex. Nature 436:801–806.

Hafting T, Fyhn M, Bonnevie T, Moser MB, Moser EI. 2008. Hippocampus-independent phase precession in entorhinal grid cells. Nature 453:1248–1252.

Hargreaves EL, Rao G, Lee I, Knierim JJ. 2005. Major dissociation between medial and lateral entorhinal input to dorsal hippocampus. Science 308:1792–1794.

Hasselmo ME. 2009. A model of episodic memory: mental time travel along encoded trajectories using grid cells. Neurobiol Learn Mem 92:559–573.

Hasselmo ME, Giocomo LM, Zilli EA. 2007. Grid cell firing may arise from interference of theta frequency membrane potential oscillations in single neurons. Hippocampus 17:1252–1271.

Heys JG, Giocomo LM, Hasselmo ME. 2010. Cholinergic modulation of the resonance properties of stellate cells in layer II of medial entorhinal cortex. J Neurophysiol 104:258–270.

Jeewajee A, Barry C, O'Keefe J, Burgess N. 2008. Grid cells and theta as oscillatory interference: electrophysiological data from freely moving rats. Hippocampus 18:1175–1185.

Klink R, Alonso A. 1993. Ionic mechanisms for the subthreshold oscillations and differential electroresponsiveness of medial entorhinal cortex layer II neurons. J Neurophysiol 70:144–157.

Koenig J, Linder AN, Leutgeb JK, Leutgeb S. 2011. The spatial periodicity of grid cells is not sustained during reduced theta oscillations. Science 332:592–595.

Kropff E, Treves A. 2008. The emergence of grid cells: intelligent design or just adaptation? Hippocampus 18:1256–1269.

Magee JC. 1998. Dendritic hyperpolarization-activated currents modify the integrative properties of hippocampal CA1 pyramidal neurons. J Neurosci 18:7613–7624.

Magistretti J, Alonso A. 1999. Slow voltage-dependent inactivation of a sustained sodium current in stellate cells of rat entorhinal cortex layer II. Ann N Y Acad Sci 868:84–87.

McNaughton BL, Battaglia FP, Jensen O, Moser EI, Moser MB. 2006. Path integration and the neural basis of the 'cognitive map'. Nat Rev Neurosci 7:663–678.

Moser EI, Moser MB. 2008. A metric for space. Hippocampus 18:1142–1156.

Navratilova Z, Giocomo LM, Fellous JM, Hasselmo ME, McNaughton BL. 2011. Phase precession and variable spatial scaling in a periodic attractor map model of medial entorhinal grid cells with realistic after-spike dynamics. Hippocampus (in press).

Nolan MF, Dudman JT, Dodson PD, Santoro B. 2007. HCN1 channels control resting and active integrative properties of stellate cells from layer II of the entorhinal cortex. J Neurosci 27:12440–12451.

O'Keefe J, Burgess N, Donnett JG, Jeffery KJ, Maguire EA. 1998. Place cells, navigational accuracy, and the human hippocampus. Philos Trans R Soc Lond B Biol Sci 353:1333–1340.

Remme MW, Lengyel M, Gutkin BS. 2009. The role of ongoing dendritic oscillations in single-neuron dynamics. PLoS Comput Biol 5:e1000493.

Rowland DC, Weible A, Wickersham I, Wu H, Seung H, Mayford MR, Witter MP, Kentros CG. 2011. Quantitative mapping of

monosynaptic inputs to entorhinal layer II neurons via transgenically-targeted rabies virus suggests a strong direct projection from hippocampal area CA2. Soc Neurosci Abstr 37:513.03.

Sargolini F, Fyhn M, Hafting T, McNaughton BL, Witter MP, Moser MB, Moser EI. 2006. Conjunctive representation of position, direction, and velocity in entorhinal cortex. Science 312:758–762.

Sharp PE. 1996. Multiple spatial/behavioral correlates for cells in the rat postsubiculum: multiple regression analysis and comparison to other hippocampal areas. Cereb Cortex 6:238–259.

Shay CF, Boardman IS, Hasselmo ME. 2010. Comparison of resonance and subthreshold membrane potential oscillation properties in whole cell patch recordings in slices of rat medial and lateral entorhinal cortex. Soc Neurosci Abstr 36:101.23.

Steffanach HA, Witter M, Moser MB, Moser EI. 2005. Spatial memory in the rat requires the dorsolateral band of the entorhinal cortex. Neuron 45:301–313.

Storm JF. 1989. An after-hyperpolarization of medium duration in rat hippocampal pyramidal cells. J Physiol 409:171–190.

Tahvildari B, Alonso A. 2005. Morphological and electrophysiological properties of lateral entorhinal cortex layers II and III principal neurons. J Comp Neurol 491:123–140.

Taube JS, Bassett JP. 2003. Persistent neural activity in head direction cells. Cereb Cortex 13:1162–1172.

Taube JS, Muller RU, Ranck JB Jr. 1990. Head-direction cells recorded from the postsubiculum in freely moving rats. I. Description and quantitative analysis. J Neurosci 10:420–435.

Traub RD, Wong RK, Miles R, Michelson H. 1991. A model of a CA3 hippocampal pyramidal neuron incorporating voltage-clamp data on intrinsic conductances. J Neurophysiol 66:635–650.

Welinder PE, Burak Y, Fiete IR. 2008. Grid cells: the position code, neural network models of activity, and the problem of learning. Hippocampus 18:1283–1300.

White JA, Budde T, Kay AR. 1995. A bifurcation analysis of neuronal subthreshold oscillations. Biophys J 69:1203–1217.

Witter MP, Moser EI. 2006. Spatial representation and the architecture of the entorhinal cortex. Trends Neurosci 29:671–678.

Witter MP, Groenewegen HJ, Lopes da Silva FH, Lohman AH. 1989. Functional organization of the extrinsic and intrinsic circuitry of the parahippocampal region. Prog Neurobiol 33:161–253.

Yoganarasimha D, Rao G, Knierim JJ. 2011. Lateral entorhinal neurons are not spatially selective in cue-rich environments. Hippocampus 21:1363–1374.

Yoshida M, Hasselmo ME. 2009. Persistent firing supported by an intrinsic cellular mechanism in a component of the head direction system. J Neurosci 29:4945–4952.

Yoshida M, Giocomo LM, Boardman I, Hasselmo ME. 2011. Frequency of subthreshold oscillations at different membrane potential voltages in neurons at different anatomical positions on the dorsoventral axis in the rat medial entorhinal cortex. J Neurosci 31:12683–12694.

Zilli EA, Hasselmo ME. 2010. Coupled noisy spiking neurons as velocity-controlled oscillators in a model of grid cell spatial firing. J Neurosci 30:13850–13860.

Zilli EA, Yoshida M, Tahvildari B, Giocomo LM, Hasselmo ME. 2009. Evaluation of the oscillatory interference model of grid cell firing through analysis and measured period variance of some biological oscillators. PLoS Comput Biol 5:e1000573.